Rapid cloud removal of dimethyl sulfide oxidation products limits SO_2 and cloud condensation nuclei production in the marine atmosphere

Gordon A. Novak[a,1,2], Charles H. Fite[b], Christopher D. Holmes[b], Patrick R. Veres[c], J. Andrew Neuman[c,d], Ian Faloona[e], Joel A. Thornton[f], Glenn M. Wolfe[g], Michael P. Vermeuel[a,3], Christopher M. Jernigan[a], Jeff Peischl[c,d], Thomas B. Ryerson[c,4], Chelsea R. Thompson[c,d], Ilann Bourgeois[c,d], Carsten Warneke[c,d], Georgios I. Gkatzelis[c,d,5], Mathew M. Coggon[c,d], Kanako Sekimoto[h], T. Paul Bui[i], Jonathan Dean-Day[j], Glenn S. Diskin[k], Joshua P. DiGangi[k], John B. Nowak[k], Richard H. Moore[k], Elizabeth B. Wiggins[k], Edward L. Winstead[k], Claire Robinson[k], K. Lee Thornhill[k], Kevin J. Sanchez[k], Samuel R. Hall[l], Kirk Ullmann[l], Maximilian Dollner[m], Bernadett Weinzierl[m], Donald R. Blake[n], and Timothy H. Bertram[a,6]

[a]Department of Chemistry, University of Wisconsin–Madison, Madison, WI 53706; [b]Department of Earth, Ocean, and Atmospheric Science, Florida State University, Tallahassee, FL 32306; [c]National Oceanic and Atmospheric Administration Chemical Sciences Laboratory, Boulder, CO 80305; [d]Cooperative Institute for Research in Environmental Sciences, University of Colorado Boulder, Boulder, CO 80309; [e]Department of Land, Air and Water Resources, University of California, Davis, CA 95616; [f]Department of Atmospheric Science, University of Washington, Seattle, WA 98195; [g]Atmospheric Chemistry and Dynamics Laboratory, NASA Goddard Space Flight Center, Greenbelt, MD 20771; [h]Graduate School of Nanobioscience, Yokohama City University, 2360027 Yokohama, Japan; [i]NASA Ames Research Center, Mountain View, CA 94035; [j]Bay Area Environment Research Institute, Moffett Field, CA 94035; [k]NASA Langley Research Center, Hampton, VA 23681; [l]Atmospheric Chemistry Observations and Modeling Laboratory, National Center for Atmospheric Research, Boulder, CO 80301; [m]Faculty of Physics, Aerosol Physics, and Environmental Physics, University of Vienna, 1090 Vienna, Austria; and [n]Department of Chemistry, University of California, Irvine, CA 92617

Edited by Patricia K. Quinn, National Oceanic and Atmospheric Administration Pacific Marine Environmental Laboratory, Seattle, WA, and accepted by Editorial Board Member Mark Thiemens September 2, 2021 (received for review June 9, 2021)

Oceans emit large quantities of dimethyl sulfide (DMS) to the marine atmosphere. The oxidation of DMS leads to the formation and growth of cloud condensation nuclei (CCN) with consequent effects on Earth's radiation balance and climate. The quantitative assessment of the impact of DMS emissions on CCN concentrations necessitates a detailed description of the oxidation of DMS in the presence of existing aerosol particles and clouds. In the unpolluted marine atmosphere, DMS is efficiently oxidized to hydroperoxymethyl thioformate (HPMTF), a stable intermediate in the chemical trajectory toward sulfur dioxide (SO_2) and ultimately sulfate aerosol. Using direct airborne flux measurements, we demonstrate that the irreversible loss of HPMTF to clouds in the marine boundary layer determines the HPMTF lifetime (τ_{HPMTF} < 2 h) and terminates DMS oxidation to SO_2. When accounting for HPMTF cloud loss in a global chemical transport model, we show that SO_2 production from DMS is reduced by 35% globally and near-surface (0 to 3 km) SO_2 concentrations over the ocean are lowered by 24%. This large, previously unconsidered loss process for volatile sulfur accelerates the timescale for the conversion of DMS to sulfate while limiting new particle formation in the marine atmosphere and changing the dynamics of aerosol growth. This loss process potentially reduces the spatial scale over which DMS emissions contribute to aerosol production and growth and weakens the link between DMS emission and marine CCN production with subsequent implications for cloud formation, radiative forcing, and climate.

dimethyl sulfide | cloud condensation nuclei | sulfate aerosol | cloud processing | marine sulfur

The oceanic emission of dimethyl sulfide (DMS; CH_3SCH_3) is the largest natural source of reduced sulfur to the atmosphere (1, 2). The oxidation of DMS ultimately leads to the production of sulfuric acid (H_2SO_4) and methane sulfonic acid (MSA; CH_3SO_3H), which contribute to new particle formation and growth (3–6). Direct observations of the full suite of DMS oxidation products are limited, making it challenging to interpret the large variability in estimates of global sulfur dioxide (SO_2) yields (31 to 98%), in which SO_2 is an immediate precursor to sulfate aerosol (SO_4^{2-}) (3, 7). An incomplete representation of DMS oxidation in global models contributes to uncertainty in estimates of the impact of DMS emissions on cloud condensation nuclei (CCN) and climate (7–9), the utility of ice core records of MSA as proxies for historical sea ice extent (10), and the use of MSA and MSA-to-sulfate ratios as a proxy of preindustrial temperature and sulfur emissions (11–14). Uncertainties in the budget of preindustrial aerosols, including those from DMS oxidation, are the largest source of uncertainty in current estimates of radiative forcing caused by the aerosol indirect effect (9).

The recent discovery of hydroperoxymethyl thioformate (HPMTF; $HOOCH_2SCHO$), a globally ubiquitous DMS oxidation product, necessitates revisiting DMS oxidation mechanisms (15–17). HPMTF is produced by the isomerization of the methylthiomethylperoxy radical ($CH_3SCH_2OO\bullet$), which is the primary product of DMS hydrogen abstraction by OH. This isomerization process competes with the bimolecular chemistry

Author contributions: G.A.N., C.H.F., C.D.H., P.R.V., I.F., T.B.R., and T.H.B. designed research; G.A.N., C.H.F., C.D.H., P.R.V., J.A.N., I.F., J.A.T., G.M.W., M.P.V., C.M.J., J.P., T.B.R., C.R.T., I.B., C.W., G.I.G., M.M.C., K.S., T.P.B., J.D.-D., G.S.D., J.P.D., J.B.N., R.H.M., E.B.W., E.L.W., C.R., K.L.T., K.J.S., S.R.H., K.U., M.D., B.W., D.R.B., and T.H.B. performed research; G.A.N., C.H.F., C.D.H., P.R.V., J.A.N., I.F., J.A.T., G.M.W., M.P.V., C.M.J., J.P., T.B.R., C.R.T., I.B., C.W., G.I.G., M.M.C., K.S., T.P.B., J.D.-D., G.S.D., J.P.D., J.B.N., R.H.M., E.B.W., E.L.W., C.R., K.L.T., K.J.S., S.R.H., K.U., M.D., B.W., D.R.B., and T.H.B. contributed new reagents/analytic tools; G.A.N., C.H.F., C.D.H., P.R.V., J.A.N., I.F., J.A.T., G.M.W., M.P.V., C.M.J., J.P., T.B.R., C.R.T., I.B., C.W., G.I.G., M.M.C., K.S., T.P.B., J.D.-D., G.S.D., J.P.D., J.B.N., R.H.M., E.B.W., E.L.W., C.R., K.L.T., K.J.S., S.R.H., K.U., M.D., B.W., D.R.B., and T.H.B. analyzed data; and G.A.N., C.H.F., C.D.H., and T.H.B. wrote the paper.

The authors declare no competing interest.

This article is a PNAS Direct Submission. P.K.Q. is a guest editor invited by the Editorial Board.

[1]Present address: Cooperative Institute for Research in Environmental Sciences, University of Colorado Boulder, Boulder, CO 80309.

[2]Present address: National Oceanic and Atmospheric Administration Chemical Sciences Laboratory, Boulder, CO 80305.

[3]Present address: Department of Soil, Water, and Climate, University of Minnesota Twin Cities, St. Paul, MN 55108.

[4]Present address: Scientific Aviation, Boulder, CO 80301.

[5]Present address: Institute of Energy and Climate Research, IEK-8: Troposphere, 52428 Jülich, Germany.

[6]To whom correspondence may be addressed. Email: timothy.bertram@wisc.edu.

This article contains supporting information online at https://www.pnas.org/lookup/suppl/doi:10.1073/pnas.2110472118/-/DCSupplemental.

Published October 11, 2021.

Significance

Ocean emissions of dimethyl sulfide (DMS) are a major precursor for the production and growth of aerosol particles, which can act as seeds for the formation of cloud droplets in the marine atmosphere with the subsequent impacts on Earth's climate. Global aircraft observations indicate that DMS is efficiently oxidized to hydroperoxymethyl thioformate (HPMTF), a previously unrecognized molecule, which necessitates revisiting DMS oxidation chemistry in the marine atmosphere. We show through ambient observations and global modeling that a dominant loss pathway for HPMTF is uptake into cloud droplets. This loss process short circuits gas-phase oxidation and significantly alters the dynamics of aerosol production and growth in the marine atmosphere.

of $CH_3SCH_2OO\bullet$, which produces SO_2 at high yield. Veres et al. determined that HPMTF is a dominant oxidation product of DMS, yet the atmospheric fate of HPMTF was unknown. Here, using direct airborne eddy covariance (EC) flux measurements, we constrain the chemical fate of HPMTF in the marine boundary layer (MBL). In the cloudy MBL, we demonstrate that the lifetime of HPMTF from cloud loss ($\tau_{HPMTF,cloud}$) is less than 2 h and is the dominant HPMTF loss pathway, thus limiting the production of SO_2. In the cloud-free MBL, HPMTF is oxidized by OH-forming SO_2, which can continue along the oxidation trajectory toward H_2SO_4 and, ultimately, CCN production. Low-altitude clouds cover nearly 50% of the global oceans in the annual mean, with stratus and stratocumulus alone covering about 35% of the oceans (18). In some regions, like the eastern subtropical oceans, stratus and stratocumulus coverage reaches 60% (19). Given that low-level clouds are a persistent feature of the marine atmosphere, it is likely that the cloud loss of soluble species within the MBL is a significant component of reactive trace gas budgets. To assess the global significance of HPMTF cloud loss on marine sulfur chemistry, we use a global, atmospheric, and chemical transport model with a method of incorporating cloud chemistry, which accounts for the entrainment of gases into clouds and fractional cloud cover in the chemical rate expression (18).

Results and Discussion

Airborne Flux Observations Reveal Efficient Cloud Loss of HPMTF. In situ airborne observations of HPMTF mixing ratios and vertical fluxes were acquired during the NASA Atmospheric Tomography (ATom) and Student Airborne Research Program (SARP) 2019 missions on the NASA DC-8 research aircraft. Here, we focus our analysis on two representative flights: 1) a SARP flight, conducted off the coast of Southern California, within a stratocumulus cloud topped MBL on July 17, 2019, and 2) an ATom-4 flight, conducted over the South Pacific Ocean, within a cloud-free MBL on May 1, 2018. Fig. 1 shows vertical profiles of DMS and HPMTF mixing ratios, true color satellite imagery, and flight tracks during the ATom and SARP MBL measurements. Two salient features emerge in the vertical profiles in DMS and HPMTF: 1) For the cloudy SARP flight, complete depletion of HPMTF is observed from cloud base (360 m) to the top of the MBL (560 m), whereas DMS is well mixed throughout the MBL, and 2) the mean [HPMTF]/[DMS] ratio measured below cloud during SARP (0.05 ± 0.03 mol · mol^{-1}) is significantly smaller than that measured in the cloud-free MBL during ATom (0.8 ± 0.5 mol · mol^{-1}), for comparable solar zenith angles ($25.8 \pm 2.5°$ and $21.2 \pm 7.1°$, respectively). This suggests either enhanced HPMTF loss (L_{HPMTF}) or suppressed HPMTF production (P_{HPMTF}) due to lower OH concentrations in the cloudy MBL. Changes in [OH] below cloud are unlikely to explain this difference, as modeled [OH] is reduced by only 30% below cloud, and a reduction in P_{HPMTF} would be partially offset by a reduction in L_{HPMTF} from reactions with OH (see *SI Appendix*, Table S5 for a full list of reactions contributing to HPMTF production and loss). Nitric oxide (NO) mixing ratios were similar between the regions (8 parts per trillion [ppt] during the clear sky ATom flight and 7 ppt during the cloudy SARP flight), indicating that the bimolecular chemistry which competes with HPMTF formation was comparable. We therefore expect the difference in [HPMTF]/[DMS] to be driven by a large additional L_{HPMTF} in the cloudy MBL case.

True color satellite imagery (Fig. 1*C*) and forward-facing camera footage (*SI Appendix*, Fig. S1) during the SARP flight reveal semiorganized, horizontal, and convective roll structures in the stratocumulus-topped MBL, visible as cloud streets with a period of ca. 7 km. This mesoscale convective structure is a common feature of marine stratocumulus systems and is characterized by counter-rotating horizontal vortices generating updrafts in which the clouds form and downdrafts of cloud-processed air between, shown schematically in Fig. 2*A* (19, 20). This structure is reflected in the time series (Fig. 2*B*) of both shortwave radiation (here shown as the photolysis rate of ozone, J_{O3}) and the vertical wind speed (w), in which J_{O3} is enhanced in the cloud-free regions and w is negative (indicating a downdraft). The impact of the convective structure is clearly distinguishable in HPMTF, which is depleted in the downdrafts in which the air has recently passed through a cloud, indicative of irreversible HPMTF loss to cloud droplets (Fig. 2*C*). Based on the response of [HPMTF] to overhead clouds shown in Fig. 2*C*, we expect the aircraft measurements of the vertical flux of HPMTF to be positive, despite the absence of an entrainment flux at cloud top because of the negligible difference in concentration between the MBL top and overlying free troposphere and the negative flux at the surface due to dry deposition. The contribution of convective roll structures on new particle formation (21) and surface heat and momentum fluxes have been demonstrated previously (19, 20), but the influence of these boundary layer dynamics on the concentration and vertical transport of reactive chemical species have not previously been considered. Observations from high–time response in situ airborne instruments provide a unique opportunity to quantitatively determine the loss rate of soluble reactive gases to clouds.

Vertical fluxes of HPMTF during SARP were directly determined in the stratocumulus-topped MBL at three altitudes (170, 180, and 255 m) using the EC technique with the continuous wavelet transform (CWT) method described further in the *Materials and Methods* and the *SI Appendix*. Mean ($\pm 1\sigma$) HPMTF mixing ratios for these segments were 4.1 ± 1.7, 4.4 ± 1.8, and 3.7 ± 1.7 ppt, respectively. Observed HPMTF vertical fluxes (F_{HPMTF}) at each altitude were 0.20 ± 0.05, 0.23 ± 0.09, and 0.20 ± 0.05 ppt · m · s^{-1}. For comparison, the HPMTF surface flux (−0.04 ppt · m · s^{-1}, where a negative flux indicates deposition) was calculated from the mean MBL [HPMTF] and the average wind speed adjusted surface deposition velocity (v_d) measured from Scripps Pier (22), discussed further in *SI Appendix*, section S4. The large, positive fluxes measured at flight altitude together with the low-HPMTF mixing ratios implies a significant overhead HPMTF loss process. The measured flux cannot be sustained by entrainment from the free troposphere as [HPMTF] is near zero in both the free troposphere and the cloudy fraction at the top of the MBL, leading to a negligible free tropospheric entrainment flux for HPMTF. The vertical profile of the mixing ratio normalized flux (F_{HPMTF}/[HPMTF]) shown in Fig. 3*C* highlights the process difference in loss rates aloft between the cloudy and clear sky cases. In the stratocumulus-topped MBL, the extrapolation of the linear flux profile to cloud base (z_{cb}) permits the calculation of an exchange velocity (v_{ex}) between the subcloud (sc) and cloud-filled regions of the MBL ($F_{\mathrm{HPMTF},z_{cb}} \times ([\mathrm{HPMTF}]_{sc} - [\mathrm{HPMTF}]_{cld})^{-1} = v_{ex} = 8.6$ cm · s^{-1}), where the HPMTF concentration in the cloud-filled region ($[\mathrm{HPMTF}]_{cld}$) is near zero. The linear extrapolation of the flux profile is justified as the chemical production and loss terms of HPMTF are constant in the well-mixed boundary layer, meaning

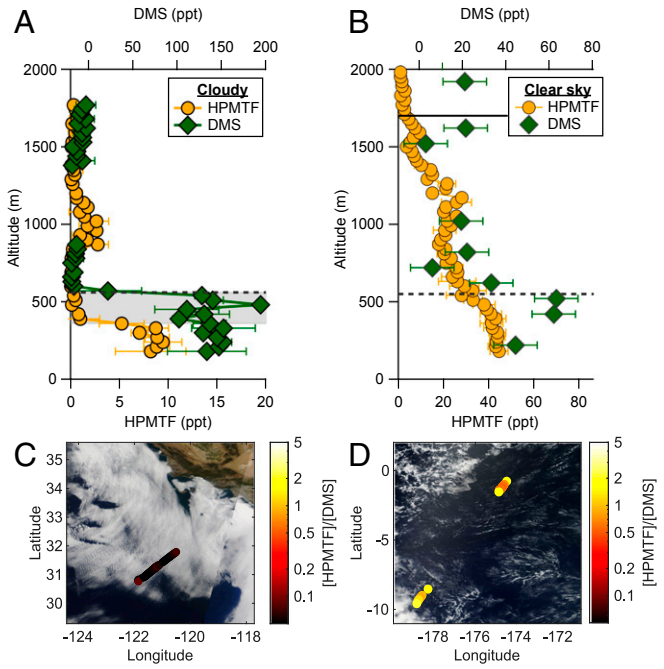

Fig. 1. Vertical profiles of DMS and HPMTF mixing ratios under cloudy (*A*) and clear sky conditions (*B*) observed during the SARP and ATom research flights, respectively. The gray shaded region in *A* represents the cloudy altitudes in the MBL. The horizontal dashed lines in *A* and *B* indicate the boundary layer height. The solid line in *B* indicates the BuL height. The SARP vertical profile is taken from the ascent at the end of the flux period, and the ATom profile is taken from the descent at the start of the second set of flux legs. *C* and *D* show the research flight path colored by the observed [HPMTF]/[DMS] ratio overlaid on true color images from Moderate Resolution Imaging Spectroradiometer Terra for the SARP (*C*) and ATom (*D*) flights, respectively. [HPMTF]/[DMS] in *C* is plotted for below cloud periods only and for altitudes below 1,500-m periods in *D*.

only the exchange terms at the ocean surface and cloud base boundaries control the shape of the flux profile. The cloud base flux ($F_{\mathrm{HPMTF},\,z_{cb}}$) is a measure of the net flux across the cloud base and, therefore, includes any potential HPMTF flux term from the evaporation of cloud droplets turbulently mixed into the subcloud region from the cloud layer.

Our observations indicate that HPMTF is strongly depleted in cloud-processed air. For highly soluble species with irreversible uptake, the loss to cloud droplets occurs at the diffusion limit, resulting in very short in-cloud lifetimes (<5 s) (23) for typical stratocumulus cloud drop diameters and concentrations [d = 15 μm, N_d = 75 $\mathrm{cm^{-3}}$ (24)]. If the average residence time of air within stratocumulus clouds is at least comparable to the in-cloud HPMTF loss rate (18) and HPMTF irreversibly reacts within the cloud droplet, we expect cloud uptake to be a significant term in the HPMTF budget. The uptake of select, isoprene-derived hydroxy nitrates to liquid aerosol has recently been shown to account for a significant global NO_x sink, demonstrating the importance of water-mediated multiphase chemistry (25). Despite the critical importance of clouds in regulating reactive trace gases, we are not aware of any direct measurements of the loss rate of soluble molecules to stratocumulus clouds in the MBL to constrain the timescales for the mixing of an airmass into the cloud layer.

Using our airborne flux measurements, we can estimate the mean residence time of MBL air in clouds (T_{cld}) as $T_{\mathrm{cld}} = d_{\mathrm{cld}} \times (v_{ex})^{-1}$, where d_{cld} is the cloud thickness ($d_{\mathrm{cld}} = z_i - z_{cb}$ = 200 m, where z_i is the boundary layer depth, determined from the vertical gradients of potential temperature, wind speed, and mixing ratios of water vapor, DMS, and HPMTF), and v_{ex} is the measured v_{ex} between the subcloud and cloud-filled regions of the MBL. Using this approach, we derive a mean in-cloud residence time of 0.64 ± 0.33 h. These calculations are largely consistent with estimated stratocumulus residence times in the range of 0.25 to 0.66 h (26–29). Results from a large eddy simulation coupled to a trajectory–ensemble model found that individual turbulent air parcels within a nonprecipitating, stratocumulus-topped MBL have a modal cloud residence time of 0.25 h (26–29). Similarly, we can calculate the lifetime of HPMTF in the subcloud region with respect to mixing and subsequent loss in the cloud-filled region as $\tau_{\mathrm{mix,\,cld}} = z_{cb} \times (v_{ex})^{-1}$. Using the measured v_{ex} derived above, we determine $\tau_{\mathrm{mix,\,cld}}$ to be 1.2 ± 0.6 h.

The vertical flux of HPMTF was also assessed under clear sky conditions during ATom. We use data from the ATom-4 campaign on May 1, 2018, as a case study because of the high-HPMTF mixing ratios and the presence of multiple steady flight legs within the boundary layer, which enables the analysis of the vertical flux profile. The near-surface vertical structure in this region was comprised of a cloud-free, well-mixed, and turbulent MBL with a height of ∼550 m. At the MBL top, there was a weak inversion separating the MBL from a stably stratified buffer layer (BuL) up to a height of 1,700 m containing sparse fair weather cumulus clouds, which is a common structure in tropical trade wind regimes (30–32). Mixing time in the BuL has been estimated to be ∼30 h, compared to less than 1 h in the well-mixed MBL, indicating that the two layers are distinct despite the weak inversion separating them (33). HPMTF EC fluxes were calculated for four sequential flux legs (L1 to L4) at altitudes of 180, 180, 390, and 570 m, respectively, in which the 570 m leg was in the bottom of the BuL. Mean HPMTF mixing ratios for all legs ranged between 30 to 45 ppt. Observed F_{HPMTF} at each altitude were 0.2 ± 0.1, 0.1 ± 0.05, 0.2 ± 0.05, and 0.3 ± 0.1 ppt · m · $\mathrm{s^{-1}}$. A clear sky HPMTF surface flux of –0.33 ppt · m · $\mathrm{s^{-1}}$ was calculated from the mean MBL [HPMTF] and the average, scaled surface v_{ex}. We again observe a positive flux at flight altitude, although the much higher [HPMTF] results in a significantly smaller concentration of normalized flux ($F_{[\mathrm{HPMTF}]}$/[HPMTF]) shown in Fig. 3*C*, with a magnitude consistent with entrainment of air by the BuL. The linear extrapolation of the observed flux profile from the surface to the top of the MBL (550 m) yields $F_{\mathrm{HPMTF}} = 0.6$ ppt · m · $\mathrm{s^{-1}}$, which yields an entrainment rate of air to the BuL $w_e = (F_{\mathrm{HPMTF},z_{zi}} \times (|[\mathrm{HPMTF}]_{\mathrm{MBL}} - [\mathrm{HPMTF}]_{\mathrm{BuL}}|)^{-1} = 2.9 \pm 1.4$ cm · $\mathrm{s^{-1}}$). This entrainment rate is within the range of 1.0 to 3.5 cm · $\mathrm{s^{-1}}$ observed in similar trade-wind boundary layers with overlying BuL structures, as observed here (31).

Observationally Constrained HPMTF Budget in the Marine Boundary Layer. To assess the consistency of fast cloud uptake of HPMTF, derived from our flux measurements, with our current understanding of HPMTF production and loss, we use aircraft observations to constrain the HPMTF scalar budget equation (Eq. 1):

$$\frac{\partial[\mathrm{HPMTF}]}{\partial t} = P - L - A - \frac{d\langle w'[\mathrm{HPMTF}]'\rangle}{dz}, \qquad [1]$$

where the time rate of change in the concentration of HPMTF ($\frac{\partial[\mathrm{HPMTF}]}{\partial t}$) is the sum of the net in situ chemical production and loss rates of HPMTF (P and L), horizontal advection (A), and the vertical flux divergence ($\frac{d\langle w'[\mathrm{HPMTF}]'\rangle}{dz}$). Integrating Eq. 1 from the surface to cloud base (z_{cb}) and from z_{cb} to the top of the MBL (z_i) results in a coupled pair of HPMTF budget equations Eq. 2A and Eq. 3A, where the HPMTF flux at cloud base ($F_{\mathrm{HPMTF},z_{cb}} = \langle w'[\mathrm{HPMTF}]'\rangle_{z_{cb}} = 0.38 \pm 0.07$ ppt · m · $\mathrm{s^{-1}}$) is common to both equations as a source to the cloud layer and a loss from the subcloud layer. The HPMTF budget equation for the cloud layer ($z_{cb} < z < z_i$) can be written as the following:

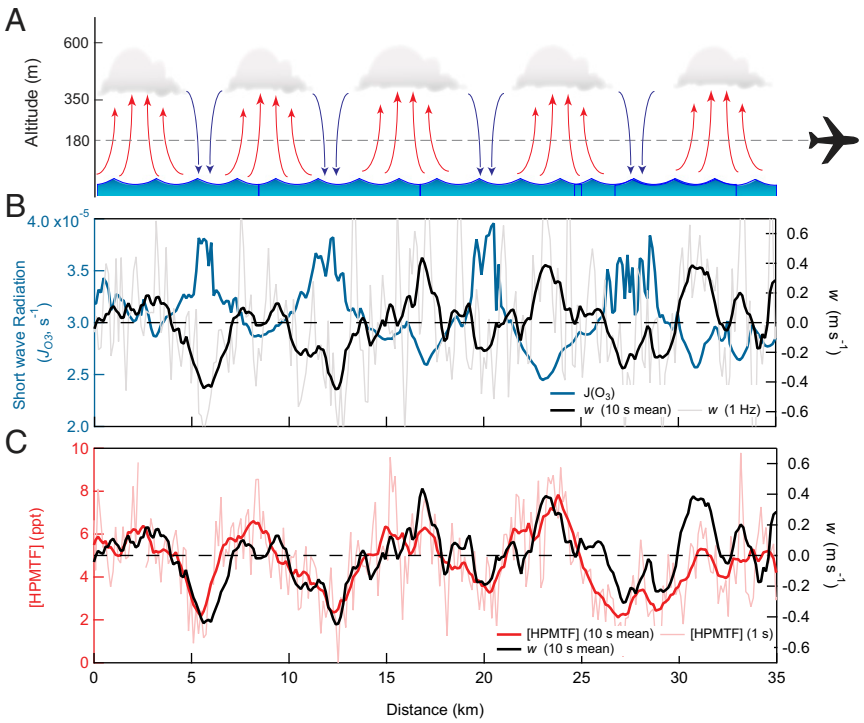

Fig. 2. (*A*) Schematic of the convective roll structure observed during the SARP research flight in the cloudy MBL with periodic cloudy and clear sky regions associated with updrafts and downdrafts, respectively. (*B*) Time series of instantaneous vertical wind speed (*w*, black) and zenith ozone photolysis rates (J_{O3}, blue), proportional to downward short wave solar radiation, indicates the cloud-free regions. (*C*) Time series of HPMTF mixing ratios ([HPMTF]) and *w* showing the depletion of HPMTF in downdraft air parcels which have experienced cloud processing. The 10-s moving average (red) and discreet 1-s time resolution (light red) HPMTF mixing ratios are included in *C*.

$$\frac{\partial[\mathrm{HPMTF}]_{\mathrm{cld}}}{\partial t} = P_{\mathrm{cld}} - A_{\mathrm{cld}} - k_{\mathrm{cld}}[\mathrm{HPMTF}]_{\mathrm{cld}} - k_{\mathrm{OH+HPMTF}}[\mathrm{OH}]_{\mathrm{cld}}[\mathrm{HPMTF}]_{\mathrm{cld}} + \frac{\langle w'[\mathrm{HPMTF}]'\rangle_{cb}}{(z_i - z_{cb})}, \quad [2A]$$

assuming that 1) [HPMTF] is in steady state in the cloud layer, a valid assumption given that $\tau_{cld} < 5$s; 2) horizontal advection is negligible; and 3) $k_{\mathrm{cld}} >>> k_{\mathrm{OH+HPMTF}} \times [\mathrm{OH}]_{\mathrm{cld}}$, a valid assumption as $k_{\mathrm{cld}} > 0.2\ \mathrm{s}^{-1}$, we can rewrite Eq. 2A solving for $[\mathrm{HPMTF}]_{\mathrm{cld}}$ as the following:

$$[HPMTF]_{cld} = (k_{cld})^{-1} \times \left(P_{cld} + \frac{\langle w'[HPMTF]'\rangle_{cb}}{(z_i - z_{cb})}\right). \quad [2B]$$

For $[\mathrm{HPMTF}]_{\mathrm{cld}}$ to be greater than the chemical ionization mass spectrometer (CIMS) detection limit (<1 ppt), P_{cld} would need to be larger than 700 ppt $\cdot$ h^{-1}, a value inconsistent with measured $[\mathrm{DMS}]_{\mathrm{cld}}$, modeled [OH], and known DMS oxidation kinetics. This confirms the near-zero HPMTF concentration measured in cloud.

The HPMTF budget equation for the subcloud layer ($z < z_{cb}$) can be written as the following:

$$\frac{\partial[\mathrm{HPMTF}]_{\mathrm{sc}}}{\partial t} = P_{\mathrm{sc}} - A_{\mathrm{sc}} - \left(k_{\mathrm{OH+HPMTF}}[\mathrm{OH}]_{\mathrm{sc}} + k_{\mathrm{het}} + \frac{v_d}{z_{cb}}\right)[\mathrm{HPMTF}]_{\mathrm{sc}} - \frac{\langle w'[\mathrm{HPMTF}]'\rangle_{cb}}{z_{cb}}, \quad [3A]$$

where k_{het} is the rate coefficient for HPMTF loss to aerosol particles. The HPMTF storage term ($\frac{\partial[HPMTF]_{sc}}{\partial t}$) in the subcloud region was calculated to be 0 ± 0.2 ppt $\cdot$ h^{-1} based on the time rate of change in [HPMTF] from legs one and three, which passed over the same location. On all three sampling legs during SARP, the along flight track component of horizontal advection in [HPMTF] was small ($\frac{\partial[HPMTF]}{\partial x} < 0.1$ ppt $\cdot$ h^{-1}). Because of limitations in the sampling strategy, we cannot constrain the cross-flight track advection term but expect it to be small because of the homogeneity of the coastal, ocean-sampling region. Taking these two assumptions, we can rearrange Eq. 3A to solve for the HPMTF production rate required to balance the HPMTF budget:

$$P_{sc} = \left(k_{OH+HPMTF}[OH]_{sc} + k_{het} + \frac{v_d}{z_{cb}}\right)[HPMTF]_{sc} + \frac{\langle w'[HPMTF]'\rangle_{cb}}{z_{cb}}. \quad [3B]$$

Concentrations of OH were determined using a 0-D chemical box model constrained by the SARP chemical and meteorological observations, as described in *SI Appendix*, section S5. The model calculated [OH] ($3.3 \pm 1 \times 10^6$ molecules $\cdot$ cm^{-3}) is consistent with prior model calculations of [OH] in the coastal MBL during summer (34, 35). For $[\mathrm{HPMTF}]_{\mathrm{sc}} = 4.4 \pm 2.1$ ppt, the OH-initiated gas-phase loss of HPMTF is estimated at 0.57 ± 0.28 ppt $\cdot$ h^{-1}, assuming that HPMTF reacts with OH at a rate comparable to the structurally similar molecule methyl thioformate (MTF; CH_3SCHO, $k_{\mathrm{OH+CH3SCHO}} = 1.1 \times 10^{-11}$ cm^3 $\cdot$ $\mathrm{molecule}^{-1}$ $\cdot$ s^{-1}), as there is no literature report of OH+HPMTF. The loss rate of HPMTF to aerosol particles (k_{het}) was calculated as $\frac{\gamma\omega S_a}{4}$, where γ is the HMPTF reactive uptake coefficient, ω is the HPMTF mean molecular speed, and S_a is the aerosol surface area. At present, γ(HPMTF) for marine aerosol is unknown. If we assume that HPMTF reacts at surfaces at a rate comparable to other soluble reactive gases ($\gamma = 0.01$), we predict an HPMTF loss rate to aerosol of 0.14 ± 0.07 ppt $\cdot$ h^{-1} for the aerosol surface area concentrations measured below cloud ($S_a = 15$ $\mu\mathrm{m}^2$ $\cdot$ cm^{-3}). There is also no experimentally measured HPMTF photolysis rate; however, the lifetime of the structurally similar molecule MTF to photolysis is 3.7 d at the equator, suggesting that the photolysis of the HPMTF aldehyde group is a minor loss term (<0.1 ppt $\cdot$ h^{-1}) in the scalar

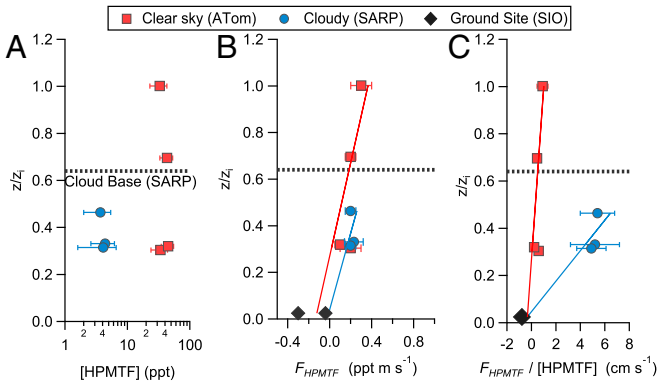

Fig. 3. Observed vertical profiles of HPMTF mixing ratios (*A*), flux (F_{HPMTF}) (*B*), and flux normalized by HPMTF mixing ratios (F_{HPMTF}/[HPMTF]) (*C*) observed under cloudy (blue) and clear (red) sky conditions during SARP and ATom, respectively. Altitudes were normalized to the boundary layer height (z_i) during each flight. HPMTF exchange velocities measured from a coastal surface site (z = 12 m) from Vermeuel et al. (22) were scaled to horizontal wind speed during each flight to calculate the surface flux (23). Solid lines are ordinary least-square best-fit lines. The dashed horizontal line on all panels indicates the height of the cloud base during the SARP flight.

budget analysis (36). HPMTF loss via deposition to the ocean surface is estimated to be 0.4 ± 0.2 ppt · h^{-1}, based on the wind speed dependent v_d. HPMTF loss to the overhead cloud layer, the final term in Eq. 3B, is determined to be 3.8 ± 0.7 ppt · h^{-1} from the extrapolated flux profile, representing the largest loss term in the HPMTF budget. Note that this term represents the net cloud loss flux and therefore includes any potential source of HPMTF from cloud droplet evaporation in the below cloud fraction of the MBL. Collectively, the total HPMTF loss rate and the corresponding HPMTF production rate in the subcloud region is estimated to be 4.9 ± 0.8 ppt · h^{-1}, where the uncertainty is calculated by propagating the 1σ variance in $[HPMTF]_{sc}$ and the uncertainty in the interpolated flux profile through Eq. **3**B.

For comparison, we can use aircraft observations to estimate HPMTF in situ production from DMS ($P_{sc} = \alpha k_{OH+DMS}[OH][DMS]$), where α is the fraction of the H abstraction reaction of DMS with OH ($k_{OH+DMS} = 4.7 \times 10^{-12}$ $cm^3 \cdot molecule^{-1} \cdot s^{-1}$) that yields HPMTF. The α term accounts for the competition between isomerization (that forms HPMTF) and bimolecular chemistry with NO, HO_2, and RO_2 (calculation of α is described in *SI Appendix*, section S5). We estimate HPMTF production (P_{HPMTF}) = 4.1 ± 1.0 ppt · h^{-1} (α = 0.76, $[DMS]_{obs}$ = 96 ppt, [OH] = 3.3×10^6 molecules · cm^{-3}). The observationally constrained HPMTF scalar budget and P_{HPMTF} calculated from DMS, therefore, close to within 1 ppt · h^{-1}. If the cloud loss term is not included in the scalar budget analysis, the HPMTF budget does not close to within 3 ppt · h^{-1}.

This analysis indicates the following: 1) rapid cloud loss for HPMTF is required to close the HPMTF budget in the cloud-topped MBL; 2) model estimates for $k_{OH+HPMTF}$ (1.1×10^{-11} $cm^3 \cdot molecule^{-1} \cdot s^{-1}$) are likely accurate to within a factor of 2, otherwise the SARP and ATom budgets would not close; and 3) cloud uptake dominates the fate of HPMTF in the stratocumulus-topped MBL ($\tau_{mix,\ cld}$ = 1.2 h and $\tau_{chem} > 5$ h). A diagram of HPMTF chemical budget terms are shown in Fig. 4. Our observations suggest that HPMTF loss to clouds is an irreversible sink for DMS-derived sulfur, in which HPMTF cloud uptake contributes to cloud droplet mass (likely as SO_4^{2-}) but quenches the potential for new particle formation, damping the link between DMS emissions and CCN concentrations.

Impact of HPMTF Cloud Loss on Global Sulfur Chemistry. To assess the global significance of HPMTF cloud loss on marine sulfur chemistry, we update the DMS and HPMTF chemistry in the Goddard Earth Observing System (GEOS)–Chem chemical transport model (version 12.9.2; ref. 37), which includes a recently developed method of incorporating cloud uptake in the chemical rate expression (18) and recent updates to marine halogen chemistry (38). Globally, we calculate that 46% of emitted DMS forms HPMTF. Prior, the observationally constrained box modeling of HPMTF production showed yields of HPMTF from DMS of 38 and 32% for ATom 3 and 4, respectively (15). In prior global modeling of the chemical fate of HPMTF using the Community Atmosphere Model with Chemistry chemical transport model, the only HPMTF loss process considered was reaction with OH (15). Using the kinetic rates described in *SI Appendix*, Table S5, we calculate the annual mean fraction of emitted sulfur from DMS, as a function of latitude, that is lost via the primary loss pathways (Fig. 5*A*). The global mean fraction of DMS-derived sulfur that is lost to clouds as HPMTF is 36%, with zonal means ranging from 10 to 50%. An additional 15% of HPMTF is lost to aerosol particles, meaning that less than half of the sulfur in HPMTF ultimately forms SO_2. During January, when DMS emissions in the Southern Hemisphere are highest, terminal sulfur loss to cloud uptake peaks at 0.58 Gg · y^{-1}, which accounts for 33% of total DMS loss. A sensitivity test taking $k_{OH+HPMTF}$ at an upper limit of 5.5×10^{-11} $cm^3 \cdot molecule^{-1} \cdot s^{-1}$ (5× base rate) shows that 31% of DMS is lost through the HPMTF cloud uptake channel compared to 36% in the base case, suggesting that uncertainty in the OH+HPMTF rate constant has little impact on this analysis.

The measurements and global model simulations presented here indicate that the cloud uptake of HPMTF is a significant, volatile sulfur loss channel, reducing the SO_2 production from DMS by 35% globally and lowering near-surface (0 to 3 km) SO_2 concentrations over the ocean by 24% (Fig. 5*B*), with consequent impacts on new particle formation from the nucleation of sulfuric acid (39). The regions with the largest percent change in SO_2 in the western ends of the major ocean gyres are regions where DMS oxidation is both a dominant local source for SO_2 and where HPMTF production and subsequent cloud loss are efficient. In nonprecipitating clouds, the condensed phase products of HPMTF aqueous phase chemistry would contribute to particle mass, following cloud processing, but would not increase particle number density (4, 40). Importantly, the proposed,

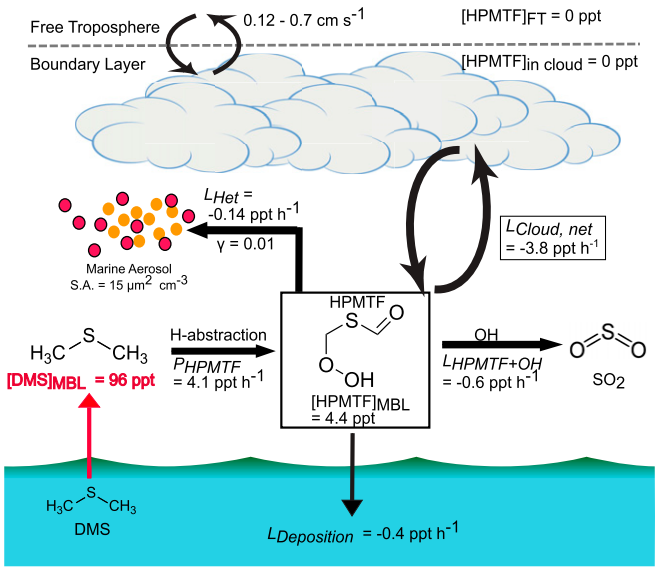

Fig. 4. The components of the HPMTF scalar budget under cloudy sky conditions, including all chemical production and loss pathways that can be directly constrained from in situ observations.

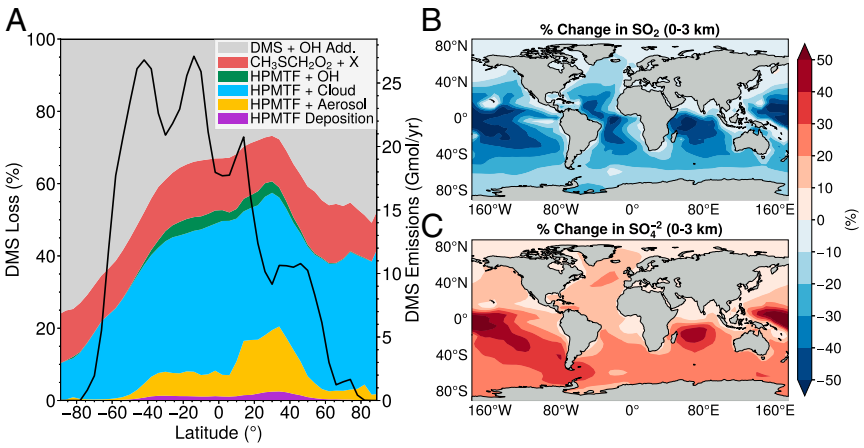

Fig. 5. (*A*) Pathways for DMS removal, as simulated by GEOS-Chem are the following: 1) OH addition and BrO reaction with DMS leading to MSA and SO_2 (gray); 2) H abstraction of DMS, primarily by OH, resulting in SO_2 production from biomolecular $CH_3SCH_2O_2$· chemistry (red), the oxidation of DMS by Cl and NO_3 radicals are an additional minor contribution; 3) HPMTF + OH gas-phase chemistry (dark green); 4) HPMTF irreversible uptake to clouds (blue); 5) HPMTF heterogeneous uptake to aerosol particles (orange); and 6) HPMTF wet and dry deposition (purple). Annual mean marine DMS emissions as a function of latitude are also shown on the right *y*-axis in black. The inclusion of cloud loss and aerosol heterogeneous uptake into the HPMTF budget results in a large reduction in [SO_2] (*B*) and large increase in [SO_4^{2-}] (*C*) for altitudes below 3 km. Results are for the model Test Case 3. The updates to the GEOS-Chem chemical mechanism used in this model implementation are detailed in *SI Appendix*, Table S4, and conditions for the model test cases are detailed in *SI Appendix*, Table S5.

prompt formation of SO_4^{2-} from aqueous HPMTF cloud chemistry dramatically increases the production rate of SO_4^{2-} in the MBL (by over 500%) and the SO_4^{2-} concentration in the marine lower atmosphere (0 to 3 km) by 22%. While the total, global sulfate burden changes only slightly, the acceleration of DMS conversion to SO_4^{2-} leads to a marked shift in the spatial distribution of sulfate in marine environments (Fig. 5*C*) and the temporal connections between DMS emissions and SO_4^{2-} formation.

The unified approach of direct ambient measurement of cloud uptake rates and global chemical modeling reveals the substantial role of clouds in regulating the budget of volatile organic molecules in the lower troposphere. We expect that cloud uptake contributes significantly to the budgets of a wide array of reactive trace gases in the atmosphere, with consequent impacts on CCN and chemical budgets in cloudy regions across the globe.

Materials and Methods

HPMTF Airborne Observations. Full details of the airborne detection of HPMTF are provided by Veres et al., with a brief description given here (15). HPMTF mixing ratios were measured on the NASA ATom and SARP campaigns with an iodide-adduct chemical ionization time-of-flight mass spectrometer (iodide CIMS, Aerodyne Research Inc.). Ambient air was sampled through a temperature, pressure, humidity, and mass flow-controlled inlet. Instrument backgrounds were determined by overflowing the inlet with scrubbed ambient air periodically, and instrument sensitivity to HPMTF was determined in postcampaign laboratory studies. HPMTF is detected as a stable adduct ion with iodide ($I\text{-}C_2H_4O_3S^-$) at a mass-to-charge ratio (*m/z*) of 234.8931. This mass is not fully resolvable from the detected product ion of dinitrogen pentoxide (N_2O_5) at the mass resolution of the instrument ($m/\Delta m$ = 5,000), and data were filtered to remove periods in which N_2O_5 potentially contributed to observed HPMTF. We note that the expected contribution of N_2O_5 to the observed HPMTF signal during the flights discussed here is negligible, as they took place during daytime under low-NO_x conditions in which N_2O_5 concentrations are low (<1 ppt). Subsequent to the publication of Veres et al., further evaluation of the calibration method identified a bias in the experiment, resulting in an overestimation in the originally reported HPMTF mixing ratios. Revised calibration experiments were performed which removed that source of bias, yielding a corrected instrument calibration factor. A corrigendum to Veres et al. has been posted detailing the updated calibration factor and the impact of those changes on the ATom observations reported in that work (15). The HPMTF mixing ratios used here for both the SARP and ATom flights reflect the updated HPMTF calibration factor. The updated ATom dataset is available through the Distributed Active Archive Center for Biogeochemical Dynamics (39, 41). The total uncertainty for HPMTF for the ATom observations was 12% + 0.4 ppt, and 1σ precision was 0.3 ppt for 1 s measurements. For the SARP flight, HPMTF uncertainty was 12% + 0.8 ppt, and 1σ precision was 0.9 ppt. DMS during SARP was measured with a proton transfer time-of-flight mass spectrometer (42). The DMS measurement from ATom used in this analysis was from whole-air samples analyzed with gas chromatography (43). Further details of the DMS measurements and other ancillary airborne measurements during ATom and SARP are listed in *SI Appendix*, Tables S1 and S2, respectively.

Airborne HPMTF Vertical Flux. The airborne vertical flux of HPMTF was computed using the EC technique using the CWT method (44–46). CWT methods for computing EC flux have emerged as a powerful technique in airborne flux studies, as it does not require homogeneity or stationarity over the averaging period and because it preserves time information, allowing for the computed flux to resolve changes over heterogeneous surfaces (44, 45, 47). All EC flux determinations for HPMTF were performed at 1-Hz time resolution. Standard flux data processing procedures and uncertainty analysis were implemented as described in *SI Appendix*, section S2. Flux averaging periods were manually selected for periods of stable aircraft altitude, pitch, and roll and to avoid data gaps in the HPMTF measurement, as described in *SI Appendix*, section S2. The SARP flight presented here was the only available flight in the MBL below cloud during the SARP or ATom missions. The ATom-4 May 1, 2018, flight was selected as a clear sky comparison case study because of the similar atmospheric conditions (e.g., SZA, O_3, NO, and aerosol surface area) compared to the SARP flight in order to limit differences in HPMTF chemistry between the flights to the presence or absence of clouds.

Global Chemical Transport Model. The chemistry of DMS and its oxidation products, including HPMTF, were simulated using the GEOS-Chem global chemical transport model (version 12.9.2). The model includes comprehensive, tropospheric oxidant chemistry, with recent updates to halogen chemistry (38) and cloud processing (18). Simulations were performed at 4 × 5° horizonal resolution with 72 vertical levels. Model sensitivity simulations were run at multiple rate constants for HPMTF+OH. The base model case uses a rate constant of 1.11×10^{-11} $cm^3 \cdot molecules^{-1} \cdot s^{-1}$. Additional simulations using HPMTF+OH of 5.5×10^{-11} $cm^3 \cdot molecules^{-1} \cdot s^{-1}$ are taken to provide an upper limit case of HPMTF gas-phase oxidation by OH, which would reduce the significance of HPMTF cloud uptake. A lower limit HPMTF+OH case was simulated using the calculated rate constant of Wu et al. of 1.40×10^{-12} $cm^3 \cdot molecules^{-1} \cdot s^{-1}$ (16). Heterogeneous uptake to both clouds and aerosols was simulated using a reactive uptake coefficient (γ) of 0.01. Model sensitivity simulations were also performed with and without HPMTF heterogeneous uptake to clouds and aerosols. A full description of the GEOS-Chem model implementation, sensitivity simulations, and model comparison to the ATom observations are provided in *SI Appendix*, sections S6–S8.

Data Availability. Merged airborne observation data from the ATom campaign is published through the Distributed Active Archive Center for Biogeochemical

Dynamics (DAAC) (ref. 41; https://doi.org/10.3334/ORNLDAAC/1925). HPMTF observations during ATom are published through DAAC at https://doi.org/10.3334/ORNLDAAC/1921 (48). All data from the 2019 SARP mission is archived in the Airborne Science Data for Atmospheric Composition database at https://www-air.larc.nasa.gov/cgi-bin/ArcView/sarp.2019. Source code for the GEOS-chem cloud processing model is available in Zenodo at https://zenodo.org/record/3959279#.YUIyKbhKg2w. All other study data are included in the article and/or *SI Appendix*.

ACKNOWLEDGMENTS. This work was supported by NSF Grant GEO AGS 1822420 and through the NSF Center for Aerosol Impacts on Chemistry of the Environment under Grant CHE 1801971. We would like to acknowledge the NASA Airborne Science Program and the NASA SARP. The authors also thank the SARP and ATom leadership and science teams and NASA DC-8 flight and ground crew for contributions to the measurements. C.H.F. and C.D.H. acknowledge support by the Future Investigators in NASA Earth and Space Science and Technology program (80NSSC19K1368) and NASA New Investigator Program (NNX16AI57G). The Langley Aerosol Research Group was supported by the NASA Tropospheric Chemistry Program (Dr. Barry Lefer, Program Manager). I.F. is supported by the California Agricultural Experiment Station funded by US Department of Agriculture, National Institute of Food and Agriculture Hatch project CA-D-LAW-2481-H. B.W. and M.D. would like to acknowledge funding from the European Research Council under the European Union's Horizon 2020 research and innovation framework program under Grant Agreement No. 640458. We would like to acknowledge Zachary Finewax, Emmanuel Assaf, and James Burkholder at the National Oceanic and Atmospheric Administration Chemical Sciences Laboratory for their work in developing a quantitative method for HPMTF calibration.

1. M. O. Andreae, Ocean-atmosphere interactions in the global biogeochemical sulfur cycle. *Mar. Chem.* **30**, 1–29 (1990).
2. T. S. Bates, B. K. Lamb, A. Guenther, J. Dignon, R. E. Stoiber, Sulfur emissions to the atmosphere from natural sourees. *J. Atmos. Chem.* **14**, 315–337 (1992).
3. E. H. Hoffmann *et al*., An advanced modeling study on the impacts and atmospheric implications of multiphase dimethyl sulfide chemistry. *Proc. Natl. Acad. Sci. U.S.A.* **113**, 11776–11781 (2016).
4. A. D. Clarke *et al*., Particle production in the remote marine atmosphere: Cloud outflow and subsidence during ACE 1. *J. Geophys. Res. Atmos.* **103**, 16397–16409 (1998).
5. S. Schobesberger *et al*., Molecular understanding of atmospheric particle formation from sulfuric acid and large oxidized organic molecules. *Proc. Natl. Acad. Sci. U.S.A.* **110**, 17223–17228 (2013).
6. M. Sipila, *et al*., The role of sulfuric acid in atmospheric nucleation. *Science* **327**, 1243–1246 (2010).
7. I. Faloona, Sulfur processing in the marine atmospheric boundary layer: A review and critical assessment of modeling uncertainties. *Atmos. Environ.* **43**, 2841–2854 (2009).
8. P. K. Quinn, T. S. Bates, The case against climate regulation via oceanic phytoplankton sulphur emissions. *Nature* **480**, 51–56 (2011).
9. K. S. Carslaw *et al*., Large contribution of natural aerosols to uncertainty in indirect forcing. *Nature* **503**, 67–71 (2013).
10. M. A. J. Curran, T. D. van Ommen, V. I. Morgan, K. L. Phillips, A. S. Palmer, Ice core evidence for Antarctic sea ice decline since the 1950s. *Science* **302**, 1203–1206 (2003).
11. E. S. Saltzman, I. Dioumaeva, B. D. Finley, Glacial/interglacial variations in methanesulfonate (MSA) in the Siple Dome ice core, West Antarctica. *Geophys. Res. Lett.* **33**, L11811 (2006).
12. M. B. Osman *et al*., Industrial-era decline in subarctic Atlantic productivity. *Nature* **569**, 551–555 (2019).
13. M. E. Hansson, E. S. Saltzman, The first Greenland ice core record of methanesulfonate and sulfate over a full glacial cycle. *Geophys. Res. Lett.* **20**, 1163–1166 (1993).
14. K. A. Read *et al*., DMS and MSA measurements in the Antarctic boundary layer: Impact of BrO on MSA production. *Atmos. Chem. Phys.* **8**, 2985–2997 (2008).
15. P. R. Veres *et al*., Global airborne sampling reveals a previously unobserved dimethyl sulfide oxidation mechanism in the marine atmosphere. *Proc. Natl. Acad. Sci. U.S.A.* **117**, 4505–4510 (2020). Correction in: *Proc. Natl. Acad. Sci. U.S.A.* **118**, e2113268118 (2021).
16. R. Wu, S. Wang, L. Wang, New mechanism for the atmospheric oxidation of dimethyl sulfide. The importance of intramolecular hydrogen shift in a CH_3SCH_2OO radical. *J. Phys. Chem. A* **119**, 112–117 (2015).
17. T. Berndt *et al*., Fast peroxy radical isomerization and OH recycling in the reaction of OH radicals with dimethyl sulfide. *J. Phys. Chem. Lett.* **10**, 6478–6483 (2019).
18. C. D. Holmes *et al*., The role of clouds in the tropospheric NOx cycle: A new modeling approach for cloud chemistry and its global implications. *Geophys. Res. Lett.* **46**, 4980–4990 (2019).
19. R. Wood, Stratocumulus clouds. *Mon. Weather Rev.* **140**, 2373–2423 (2012).
20. G. S. Young, D. R. Kristovich, M. R. Hjelmfelt, R. C. Foster, Rolls, streets, waves, and more. *Bull. Am. Meteorol. Soc.* **83**, 997–1001 (2002).
21. J. Lampilahti *et al*., Roll vortices induce new particle formation bursts in the planetary boundary layer. *Atmos. Chem. Phys.* **20**, 11841–11854 (2020).
22. M. P. Vermeuel, G. A. Novak, C. M. Jernigan, T. H. Bertram, Diel profile of hydroperoxymethyl thioformate: Evidence for surface deposition and multiphase chemistry. *Environ. Sci. Technol.* **54**, 12521–12529 (2020).
23. S. Z. Levine, S. E. Schwartz, In-cloud and below-cloud scavenging of nitric acid vapor. *Atmos. Environ.* **16**, 1725–1734 (1982).
24. N. L. Miles, J. Verlinde, E. E. Clothiaux, Cloud droplet size distributions in low-level stratiform clouds. *J. Atmos. Sci.* **57**, 295–311 (2000).
25. K. T. Vasquez *et al*., Rapid hydrolysis of tertiary isoprene nitrate efficiently removes NO_x from the atmosphere. *Proc. Natl. Acad. Sci. U.S.A.* **117**, 33011–33016 (2020).
26. G. Feingold, S. M. Kreidenweis, Y. Zhang, Stratocumulus processing of gases and cloud condensation nuclei 1. Trajectory ensemble model. *J. Geophys. Res. Atmos.* **103**, 19527–19542 (1998).
27. G. Feingold, A. McComiskey, D. Rosenfeld, A. Sorooshian, On the relationship between cloud contact time and precipitation susceptibility to aerosol. *J. Geophys. Res. Atmos.* **118**, 10544 (2013).
28. B. Stevens, G. Feingold, W. R. Cotton, R. L. Walko, Elements of the microphysical structure of numerically simulated nonprecipitating stratocumulus. *J. Atmos. Sci.* **53**, 980–1006 (1996).
29. Y. L. Kogan, Large-eddy simulation of air parcels in stratocumulus clouds: Time scales and spatial variability. *J. Atmos. Sci.* **63**, 952–967 (2006).
30. I. Faloona *et al*., Sulfur dioxide in the tropical marine boundary layer: Dry deposition and heterogeneous oxidation observed during the Pacific Atmospheric Sulfur Experiment. *J. Atmos. Chem.* **63**, 13–32 (2010).
31. S. A. Conley *et al*., Closing the dimethyl sulfide budget in the tropical marine boundary layer during the Pacific Atmospheric Sulfur Experiment. *Atmos. Chem. Phys.* **9**, 8745–8756 (2009).
32. L. M. Russell *et al*., Bidirectional mixing in an ACE 1 marine boundary layer overlain by a second turbulent layer. *J. Geophys. Res. Atmos.* **103**, 16411–16432 (1998).
33. A. Bandy *et al*., Pacific Atmospheric Sulfur Experiment (PASE): Dynamics and chemistry of the south Pacific tropical trade wind regime. *J. Atmos. Chem.* **68**, 5–25 (2011).
34. T. P. Riedel *et al*., Nitryl chloride and molecular chlorine in the coastal marine boundary layer. *Environ. Sci. Technol.* **46**, 10463–10470 (2012).
35. T. A. Crisp *et al*., Observations of gas phase hydrochloric acid in the polluted marine boundary layer. *J. Geophys. Res. Atmos.* **119**, 6897–6915 (2014).
36. I. V. Patroescu, I. Barnes, K. H. Becker, FTIR kinetic and mechanistic study of the atmospheric chemistry of methyl thiolformate. *J. Phys. Chem.* **100**, 17207–17217 (1996).
37. GEOS-Chem, version 12.9.2. https://geos-chem.seas.harvard.edu/. Accessed 27 September 2021.
38. X. Wang *et al*., The role of chlorine in global tropospheric chemistry. *Atmos. Chem. Phys.* **19**, 3981–4003 (2019).
39. A. D. Clarke, *et al*., Particle nucleation in the tropical boundary layer and its coupling to marine sulfur sources. *Science* **282**, 89–92 (1998).
40. C. J. Williamson *et al*., A large source of cloud condensation nuclei from new particle formation in the tropics. *Nature* **574**, 399–403 (2019).
41. S. C. Wofsy *et al*., ATom: Merged atmospheric chemistry, trace gases, and aerosols. https://doi.org/10.3334/ORNLDAAC/1925. Accessed 27 September 2021.
42. B. Yuan *et al*., A high-resolution time-of-flight chemical ionization mass spectrometer utilizing hydronium ions (H3O+ ToF-CIMS) for measurements of volatile organic compounds in the atmosphere. *Atmos. Meas. Tech.* **9**, 2735–2752 (2016).
43. J. J. Colman *et al*., Description of the analysis of a wide range of volatile organic compounds in whole air samples collected during PEM-tropics A and B. *Anal. Chem.* **73**, 3723–3731 (2001).
44. G. M. Wolfe *et al*., Quantifying sources and sinks of reactive gases in the lower atmosphere using airborne flux observations. *Geophys. Res. Lett.* **42**, 8231–8240 (2015).
45. G. M. Wolfe *et al*., The NASA Carbon Airborne Flux Experiment (CARAFE): Instrumentation and methodology. *Atmos. Meas. Tech.* **11**, 1757–1776 (2018).
46. C. Torrence, G. P. Compo, A practical guide to wavelet analysis. *Bull. Am. Meteorol. Soc.* **79**, 61–78 (1998).
47. P. K. Misztal *et al*., Airborne flux measurements of biogenic isoprene over California. *Atmos. Chem. Phys.* **14**, 10631–10647 (2014).
48. P. R. Veres, J. A. Neuman, T. B. Ryerson, ATom: L2 Measurements from the NOAA ToF Chemical Ionization Mass Spectrometer (CIMS). https://doi.org/10.3334/ORNLDAAC/1921.